

Full length article

Hydrogen-assisted failure in Ni-based superalloy 718 studied under in situ hydrogen charging: The role of localized deformation in crack propagation

Z. Tarzimoghdam^{a,*}, D. Ponge^{a,*}, J. Klöwer^b, D. Raabe^a^a Max-Planck-Institut für Eisenforschung GmbH, Max-Planck-Straße 1, 40237 Düsseldorf, Germany^b VDM Metals GmbH, Kleffstraße 23, 58762 Altena, Germany

ARTICLE INFO

Article history:

Received 23 November 2016

Received in revised form

20 February 2017

Accepted 20 February 2017

Available online 21 February 2017

Keywords:

Alloy 718

Hydrogen embrittlement

Planar slip

Slip localization

Hydrogen-enhanced localized plasticity

ABSTRACT

We investigated hydrogen embrittlement in Ni-based superalloy 718 by tensile testing at slow strain rate (10^{-4} s^{-1}) under continuous electrochemical hydrogen charging. Hydrogen-assisted cracking mechanisms were studied via electron backscatter diffraction (EBSD) analysis and electron channeling contrast imaging (ECCI). In order to elucidate the effects of stress or strain in the cracking mechanisms, material conditions with different strength levels were investigated, including samples in solution annealed (as water quenched) and 780 °C age-hardened states. The microstructure observations in the vicinity of the cracks enabled us to establish correlations between the microstructure, crack initiation sites, and crack propagation pathways. Fracture in the hydrogen-charged samples was dominated by localized plastic deformation. Strain-controlled transgranular cracking was caused by shear localization due to hydrogen-enhanced localized plasticity (HELP) and void nucleation and coalescence along {111} slip planes in both, the solution annealed and age-hardened materials. Stress-assisted intergranular cracking in the presence of hydrogen was only observed in the high strength age-hardened material, due to slip localization at grain boundaries, grain boundary triple junction cracking, and δ/γ -matrix interface cracking. To investigate the effect of δ -phase in crack propagation along grain boundaries, the over-aged state (aged at 870 °C) with different precipitation conditions for the δ -phase was also investigated. Observations confirmed that presence of δ -phase promotes hydrogen-induced intergranular failure by initializing micro-cracks from δ/γ interfaces.

© 2017 Acta Materialia Inc. Published by Elsevier Ltd. All rights reserved.

1. Introduction

Nickel-based superalloy 718 is widely used for critical applications under extreme conditions such as sour gas environments in the oil and gas industry, due to its room temperature strength and high aqueous corrosion resistance [1]. However, it has been shown that the alloy is rather susceptible to hydrogen embrittlement (HE), resulting in continuous efforts to understand the specific hydrogen-related damaging mechanisms in this material [2–6]. Alloy 718 is a precipitation-hardened material strengthened by an ordered body-centered tetragonal (bct) γ'' phase (primary strengthening precipitate), and an ordered face-centered cubic (fcc) γ' phase. Beside these two coherent matrix-strengthening phases, incoherent

precipitates of δ particles also tend to form at grain boundaries (GBs) [7]. Most studies have focused on the role of the precipitates in HE of alloy 718. The HE sensitivity has been mostly assessed by degradation in mechanical properties and change of fracture modes in different precipitation conditions [3–5]. Liu et al. [3] showed that the HE sensitivity of alloy 718 was minimal when all the precipitates (γ'/γ'' and δ) were dissolved. The effect of hydrogen was found to be more pronounced in case of an increased volume fraction of γ'' and even more extensive when δ -phase was present. Galliano et al. [4] reported that material devoid of these three types of intermetallic precipitates was also sensitive to HE. They attributed this observation to the higher hydrogen content and to the presence of carbides. Rezende et al. [5] showed that the degree of embrittlement increased in the precipitation-hardened state compared to the solution annealed condition. Also permeation tests have indicated that presence of precipitates lower hydrogen diffusivity and permeability [4,5].

* Corresponding author.

E-mail address: d.ponge@mpie.de (D. Ponge).

Irrespective of these pioneering studies in this field there is a lack of thorough microstructural observations in direct conjunction with hydrogen loading for better understanding the hydrogen-related mechanisms assisting damage formation in this alloy. Recently Zhang et al. [6] performed more detailed characterization of the dislocation activity related to cracking mechanism in age-hardened alloy 718. They also reported significant reduction in the tensile ductility of hydrogen pre-charged samples. The underlying failure mechanism was crack propagation along planar dislocation slip bands, but not along grain- and twin boundaries.

Generally, HE susceptibility of structural alloys is strongly influenced by their associated deformation mechanisms [8,9]. It has been reported that alloys deforming by planar slip, with a greater inherent propensity for localized deformation (e.g. due to lower stacking fault energy, coherent precipitates or short-range ordering), are more susceptible to hydrogen effects compared to materials with more homogeneously acting deformation modes [10–12]. Planar slip bands in alloy 718 have been observed by several researchers [13–15]. Presence of precipitates with an ordered crystal structure in precipitation-hardened materials or ordering of phases or alloying elements (e.g. short range ordering or short range clustering) promote deformation via planar slip. Shearing or destroying the order of precipitates by the leading dislocations results in glide plane softening. Hence, further dislocation activity is promoted along the same slip plane [16].

The hydrogen-enhanced localized plasticity (HELP) mechanism comprises effects associated with specific deformation modes arising from the presence of hydrogen. The dislocation generation rate and the average dislocation velocity are increased in the presence of hydrogen [17–19]. According to this model hydrogen lowers the dislocations interactions with elastic obstacles, which leads to reduction in shear stress for dislocation motion, hence localized deformation is promoted [20–28]. As HE occurs preferably in strain-localized regions [8], the localized slip typically observed in strained Ni-based superalloys is consequently believed to affect their HE sensitivity. Hydrogen-assisted cracking in metals and alloys can occur either by transgranular or intergranular cracking. The former has been described as a strain-controlled phenomenon occurring at high stress levels by localized plastic flow on the macroscale and the latter as a stress-controlled mechanism, which is initiated by inhibited plasticity on the microscale [29].

In this work we investigated HE of alloy 718 by in situ tensile testing under hydrogen charging placing the focus on the underlying hydrogen-related deformation mechanisms and cracking. In order to elucidate the contributions of stress or strain to the cracking mechanisms, samples with different strengths were investigated: after solution annealing (as quenched state) and after age-hardening at 780 °C. To investigate the effect of the GB δ -phase

in intergranular crack propagation, samples in over-aged condition (aged at 870 °C) with different precipitation conditions of the δ -phase, were also investigated. Hydrogen-related cracks were studied with the correlative use of electron backscatter diffraction (EBSD) and electron channeling contrast imaging (ECCI) analyses to establish correlations between the microstructure, crack initiation sites, and crack propagation pathways.

2. Experimental procedures

Table 1 presents the chemical composition of the alloy used in this study. VDM Metals GmbH, Germany supplied the material from hot forged bars in the annealed condition. The solution annealing was conducted at 1032 °C for 2 h followed by water quenching (WQ). The subsequent age-hardening was done at 780 °C for 8 h followed by air cooling (age-hardened condition). Another heat treatment was performed by aging at 870 °C for 8 h followed by air cooling (over-aged condition). Table 2 lists the different sample conditions and the corresponding heat treatments.

Tensile testing was conducted using an Instron machine, at room temperature with constant cross head speed corresponding to an initial strain rate of 10^{-4} s^{-1} . Tensile specimens with gauge dimensions of 3 mm in width, 10 mm in length, and 1 mm in thickness were cut by spark erosion and mechanically grinded. The strain values were calculated by dividing the displacement of the cross head by the initial gauge length. Three samples were tested each at air and under hydrogen charging. The experimental set-up used for in situ tensile test under hydrogen charging is explained in detail elsewhere [30]. Only the gauge portion of the specimens was subjected to hydrogen charging. Hydrogen charging was conducted electrochemically before the tensile test for 4 h and also continuously during the ongoing test in a 5% H_2SO_4 aqueous solution containing 3 g l^{-1} of NH_4SCN as a hydrogen recombination poison, at a cathodic current density of 40 mA cm^{-2} . A platinum foil was used as the counter electrode. The surface of a polished sample was observed under SEM before and directly after hydrogen charging without further surface treatment. Observations showed no surface defects caused by the hydrogen charging process.

Thermal desorption spectroscopy (TDS) was performed only on the age-hardened condition (AH-780) in order to compare the hydrogen charging modes (hydrogen pre-charging vs. in situ charging) in terms of the hydrogen content introduced into the samples. TDS samples were taken from the gauge part of the tensile samples, which were subjected to hydrogen charging. It took about 20 min to start the TD experiments after the end of hydrogen charging. TDS was conducted from 25 °C to 800 °C at a constant heating rate of 52 °C min^{-1} . The hydrogen content was determined by the cumulative hydrogen desorbed from room temperature to 300 °C. Samples for microstructural observations were cut from the gauge part of the tensile specimens, both from the surface and from the cross section (sectioned longitudinally in the middle). Observations were mainly concentrated on the surface side, and in case of the cross section of the hydrogen charged samples, were focused on the regions close to the surface (hydrogen-affected zones). Samples were prepared by mechanical grinding and polishing. Final polishing step was done with colloidal silica suspension to ensure a

Table 1
Chemical composition of the studied alloy 718 (in wt-%).

Ni	Cr	Fe	Nb	Mo	Ti	Al	Co	Si
54.49	18.7	17.04	4.96	3.02	0.93	0.55	0.09	0.05
Mn	Cu	W	C	V	N	P	B	Mg
0.03	0.03	0.03	0.02	0.02	0.007	0.005	0.004	0.001

Table 2
Different heat treatments of alloy 718 investigated in this study and the corresponding abbreviations used throughout.

Material Condition	Heat treatment
As WQ	Solution annealing at 1032 °C, 2 h/water quenching (WQ)
AH-780	Solution annealing at 1032 °C, 2 h/water quenching + Age-hardening at 780 °C, 8 h/air cooling
AH-870	Solution annealing at 1032 °C, 2 h/water quenching + Over-aging at 870 °C, 8 h/air cooling

deformation-free surface.

Microstructural observations were performed by EBSD, secondary electron (SE), backscatter electron (BSE), and ECCI. Scanning electron microscopic (SEM) analyses were done in Zeiss-Crossbeam XB 1540 FIB-SEM and Zeiss Merlin (Carl Zeiss SMT AG, Germany). The EBSD analyses were conducted at 15 kV acceleration voltage with a beam step size of 1 μm –100 nm. The Kernel average misorientation (KAM) values were calculated using first neighboring EBSD points. The KAM is a parameter that quantifies the average misorientation around a reference measurement point with respect to a defined set of nearest neighbor points and has been suggested as a measure of the geometrically necessary dislocation (GND) density [31]. Hence, it can serve to qualitatively assess the local plastic strain related to deformation gradients.

ECCI analyses were performed using a Zeiss Merlin SEM, equipped with a field emission gun and a solid state four-quadrant detector. ECCI was conducted at 30 kV acceleration voltage and working distance of approx. 6 mm. ECCI is a powerful SEM technique, which enables observation of lattice defects such as, dislocations and stacking faults as well as slip lines, twins and grain boundaries in bulk materials [32] [33]. A detailed review of the theory and application of the technique is given in Ref. [34]. It is a suitable method for investigating the correlation between dislocation structures, slip lines, and cracking on a mesoscopic scale and at a wider field of view compared to transmission electron microscopy (TEM) substructure imaging.

3. Results

Most of the results presented in this section concern the engineering alloy, age-hardened at 780 °C (section 3.1). For a better understanding of the hydrogen-related damaging mechanisms, samples in the solution annealed and over-aged conditions were also investigated and are presented in corresponding sub-sections (sections 3.2 and 3.3, respectively).

3.1. Age-hardened at 780 °C (AH-780)

The initial microstructure was austenitic, with an average grain size of 21 μm including annealing twin boundaries (Fig. 1a).

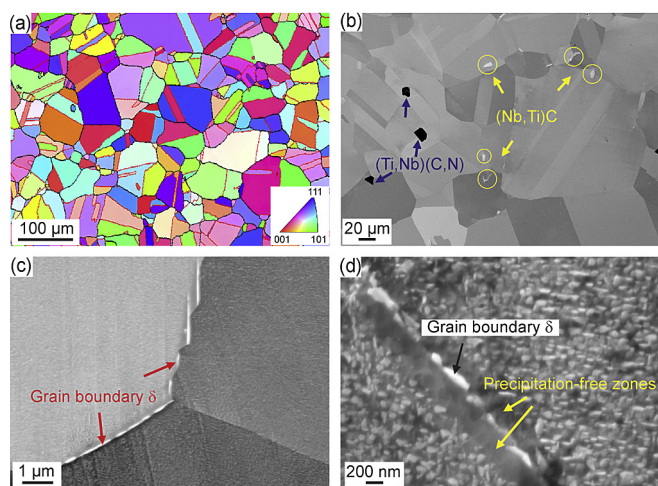


Fig. 1. Initial undeformed microstructure of AH-780 (age-hardened at 780 °C): (a) EBSD-IPF map (step size: 1 μm). The red lines indicate $\Sigma 3$ twin boundaries. (b) BSE image showing carbonitrides in the matrix, (c) and (d) BSE images showing nm-sized precipitates and grain boundary δ -phase. (IPF: Inverse pole figure). (For interpretation of the references to colour in this figure legend, the reader is referred to the web version of this article.)

Table 3

Typical precipitates in alloy 718.

Precipitate	Chemistry	Crystal structure	Position
Carbonitrides (MX)	(Ti,Nb)(C,N)	fcc ^a	matrix
γ'	$\text{Ni}_3(\text{Al,Ti})$	fcc ^a ordered, $L1_2$	matrix
γ''	Ni_3Nb	bct ^a ordered, $D0_{22}$	matrix
δ	Ni_3Nb	Orthorhombic, $D0_a$	at grain boundaries

^a fcc-face centered cubic, bct-body centered tetragonal.

Primary carbonitrides ((Ti,Nb)(C,N)) were present in the microstructure (Fig. 1b). The matrix contained nano-sized γ'/γ'' precipitates, formed during the age-hardening process. δ particles were distributed along some of the GBs (Fig. 1c and d). The presence of δ -phase led to formation of precipitation-free zones of an average extension of 200 nm on each side of the GBs, due to local depletion of Nb. Table 3 summarizes the typical precipitates present in alloy 718. Since the primary carbonitrides are not affected by the heat treatments, they are not considered as a variable between the different samples and our referring to precipitates throughout the study concerns the intermetallic phases (γ'/γ'' and δ) affected by heat treatment conditions, unless stated otherwise.

The experimental set-up chosen for in situ tensile testing under hydrogen charging is shown schematically in Fig. 2a. Fig. 2b shows engineering stress-strain curves both, with and without hydrogen charging. The yield strength (~ 1 GPa) was not affected significantly, but the elongation was decreased drastically from 45% (without hydrogen) to about 12% in the presence of hydrogen. TDS was performed immediately after the tensile test under hydrogen charging. The results were compared with a sample pre-charged with hydrogen at the same conditions, but without in situ deformation (Fig. 2c). Comparison of the TD curves and the corresponding hydrogen contents showed a clear increase in the hydrogen uptake during in situ tensile test under hydrogen charging.

3.1.1. Deformation microstructure without the presence of hydrogen

Fig. 3 shows post mortem deformation microstructures of the specimen fractured without hydrogen charging. The crystallographic texture of the tensile specimen in the vicinity of the necking region was characterized by pronounced $\langle 111 \rangle$ or $\langle 001 \rangle$ texture components parallel to the tensile axis (Fig. 3a). Strain localization was observed along slip lines and at GBs (Fig. 3b). The fracture surface was covered by dimples indicating a dominant ductile failure (Fig. 3c₁). No secondary cracks were observed on the sample surface and cross section; only at high strain levels in the necking region, cracking of the carbides and debonding along the carbides were observed (Fig. 3c_{2,c3}).

Fig. 3d₁–d₃ show ECC images of the sample deformed without the presence of hydrogen until 12% total engineering plastic strain. This is the strain level at which the samples were fractured in the presence of hydrogen. In reference, 12% straining did not induce any cracks in the uncharged sample. Deformation occurred by planar slip and multiple intersecting planar slip lines were observed (Fig. 3d₃). Trace analysis conducted by EBSD identified the slip lines along $\{111\}$ planes. High strain localization (shown in terms of bright contrast in the orientation-optimized ECC image (Fig. 3d₂)) was observed at intersections of the slip lines and GBs.

3.1.2. Hydrogen-induced cracking and fracture

Fig. 4a shows the overall fracture surface of the specimen that failed under hydrogen exposure (12% total elongation to fracture). The fracture mode in the center of the sample was ductile, dominated by dimples (Fig. 4b). The regions close to the side edges of the sample (marked with yellow lines in Fig. 4a) corresponding to the

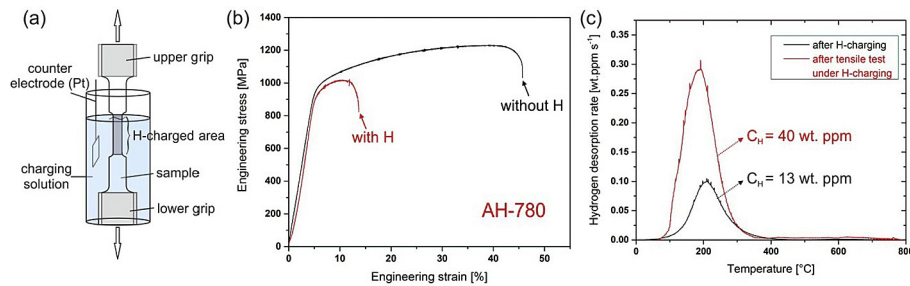


Fig. 2. (a) Schematic of the set up used for in situ tensile testing under H-charging. (b) Engineering stress-strain curves of AH-780, with and without hydrogen exposure. (c) Comparison of the TD spectra after in situ tensile test under H-charging and after pre-charging without deformation. C_H values indicate the corresponding hydrogen contents. (Heating rate = 52 °C min⁻¹).

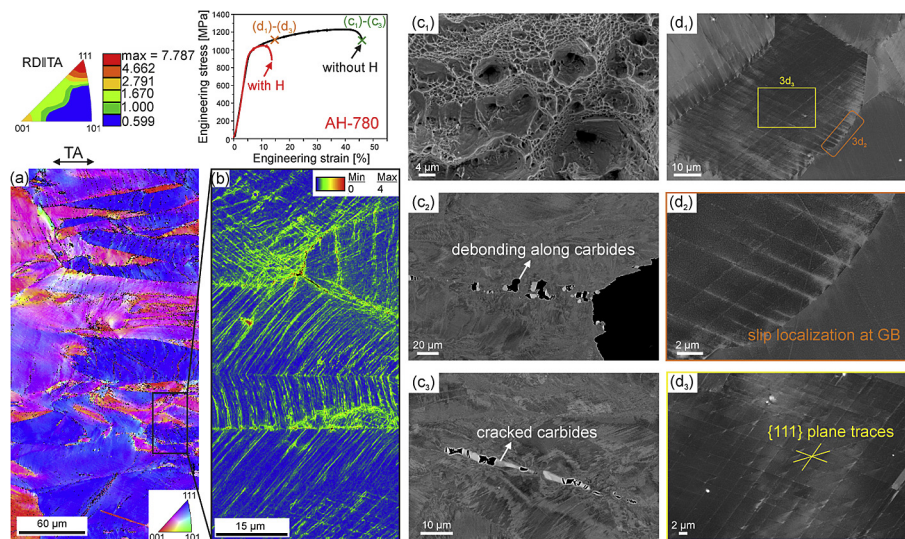


Fig. 3. Deformation microstructure of AH-780 without hydrogen exposure: (a) IPF map in the vicinity of the necking region (step size: 200 nm) and the corresponding texture, (b) higher magnification KAM map of the marked region in (a) (step size: 100 nm), (c₁) fracture surface, (c₂) and (c₃) BSE images of the fractured sample. (d₁) - (d₃) ECC images of the deformed sample till 12% strain without hydrogen exposure. The EBSD scans and the images are taken from the surface. (IPF: Inverse pole figure, TA: Tensile axis, RD: Rolling/longitudinal direction, KAM: Kernel average misorientation).

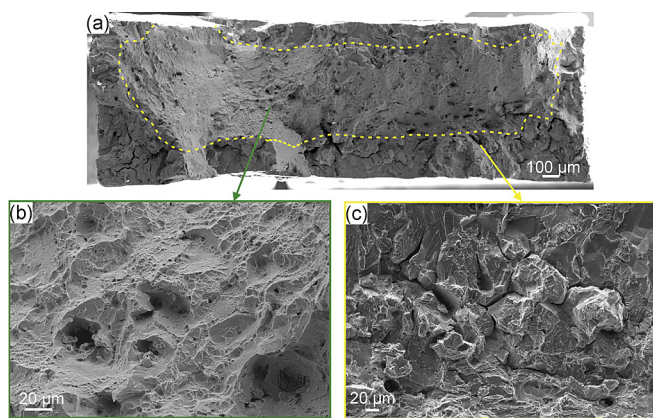


Fig. 4. (a) Fracture surface overview of AH-780, failed in the presence of hydrogen. Magnified images of: (b) central specimen area, less affected by hydrogen, and (c) specimen edge area, strongly affected by hydrogen.

hydrogen-affected area, revealed characteristics of intergranular and transgranular fracture (Fig. 4c).

More detailed microstructural observations were conducted to identify correlations between the microstructure and the crack propagation paths. Fig. 5 shows series of images of the observed

intergranular mode of cracking. Intergranular cracking was observed at GB triple junctions (Fig. 5a₁-a₃), at γ/γ GBs (Fig. 5b₁-b₃), and along GB δ-phase (Fig. 5c₁,c₂).

Combined EBSD and ECCI observations showed transgranular cracks propagating along slip lines by localized deformation (Fig. 6a₁,a₂), along alternating {111} slip planes with 'zig-zag' microfracture (Fig. 6b₁,b₂), and with growth direction on {100} planes near {110} (Fig. 6c₁,c₂).

3.2. Solution annealed, as water quenched (as WQ)

Fig. 7a shows the engineering stress-strain curves of the as WQ samples with and without hydrogen charging. As expected, the yield strength was very low, namely, only 400 MPa, prior to precipitation-hardening. ECC images of the deformed sample which was not exposed to hydrogen showed clearly a planar dislocation substructure (Fig. 7b-d). The material still showed susceptibility to HE even at this low strength level, in the solution annealed condition and thus without the presence of γ'/γ'' and δ precipitates. The elongation to fracture in the presence of hydrogen was 30%, reduced by ~70% relative to the non-hydrogen charged sample.

Fracture surfaces of the samples failed in the presence of hydrogen showed river patterns, characteristic of quasi-cleavage

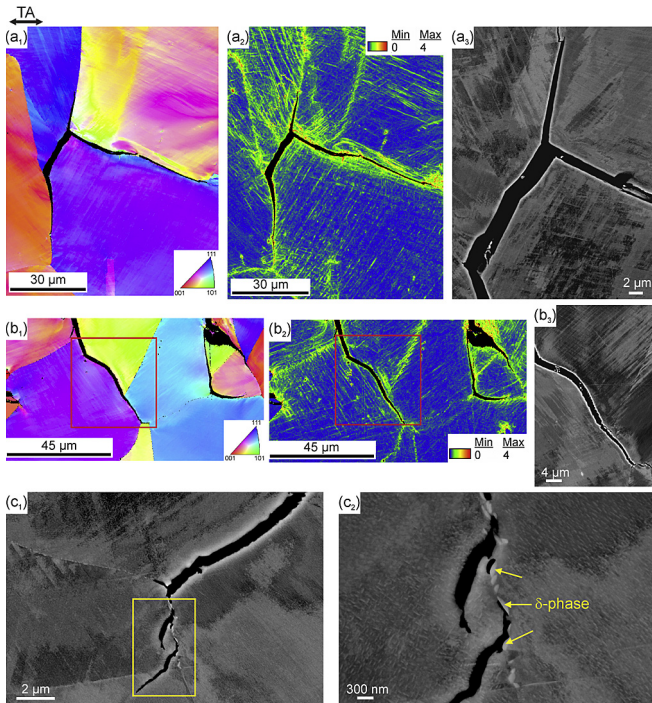


Fig. 5. Hydrogen-induced intergranular cracking in AH-780: GB triple junction cracking: (a₁) IPF map, (a₂) KAM map, (a₃) ECC image. γ/γ GB cracking: (b₁) IPF map, (b₂) KAM map, (b₃) ECC image. Cracking along GB δ -phase: (c₁), (c₂) BSE images. (EBSD step size: 200 nm). The EBSD scans and the images are taken from the surface. (TA: Tensile axis, IPF: Inverse pole figure, KAM: Kernel average misorientation).

fracture (Fig. 8a) indicating occurrence of fracture along slip planes. More detailed observations revealed that these river patterns consisted of ridges. Post mortem microstructural observations on the surface and cross section (in the hydrogen-affected zone), using combined ECCI and EBSD measurements showed the occurrence of transgranular cracking along $\{111\}$ slip planes (Fig. 8b–d). No cracking was observed along the GBs.

3.3. Age-hardened at 870 °C, over-aged (AH-870)

As mentioned above δ -phase forms at GBs during the age-hardening process. Crack propagation along δ -decorated GBs was

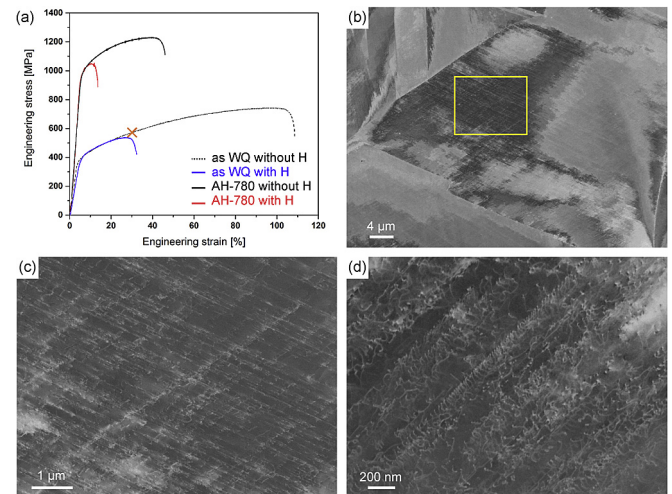


Fig. 7. (a) Engineering stress-strain curves of the as WQ sample compared with AH-780 (age-hardened at 780 °C), (b)–(d) ECC images of the as WQ sample deformed till 30% strain without hydrogen exposure (images taken from the surface).

observed in AH-780 samples failed in the presence of hydrogen (Fig. 5c₁,c₂). In order to elucidate the effect of δ -phase on intergranular cracking (excluding the influence of GBs), samples were also investigated in the over-aged condition by aging at 870 °C (AH-870). Since the characteristics of δ -phase formation depend strongly upon temperature [7], aging at 870 °C led to increased volume fraction of intergranular and intragranular δ (Fig. 9a).

Fig. 9b shows the engineering stress-strain curves with and without hydrogen charging. Since the growth of δ occurs at the expense of γ'' , aging at 870 °C caused significant decrease in strength compared to aging at 780 °C. Same as AH-780, reduction of ductility occurred by the hydrogen uptake. The ductility decreased from 65% (without hydrogen exposure) to 17% (with hydrogen exposure). Fig. 9c and d shows the deformation microstructures without the hydrogen effect. At high strain levels (where fracture occurred) no crack propagation was observed along the δ -phase, only some void formation/debonding events were found at high strain levels in the necking region (Fig. 9c). No crack/void formation developed along the δ -phase in the sample deformed till 17% strain, which is the reference strain level at which fracture took place in the presence of hydrogen (Fig. 9d).

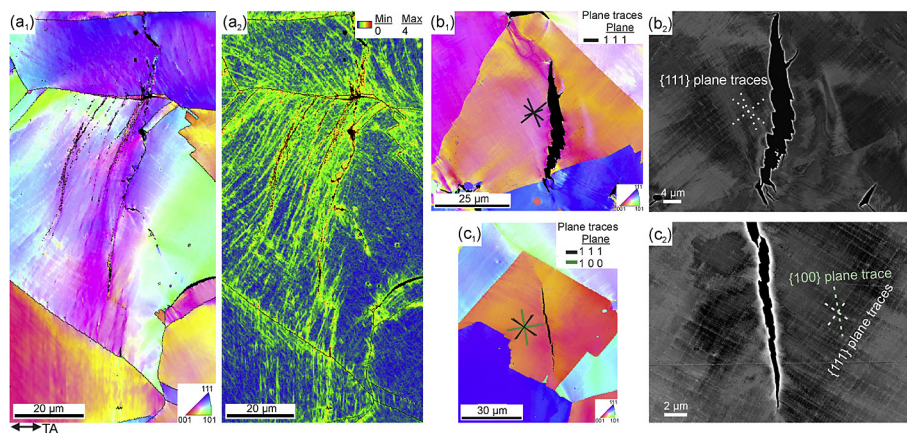


Fig. 6. Hydrogen-induced transgranular cracking in AH-780: (a₁) IPF map and (a₂) the corresponding KAM map (taken from the surface). The black lines indicate the high angle GBs. (b₁) and (c₁) IPF maps, (b₂) and (c₂) corresponding ECC images. (EBSD step size: 100 nm). (b₁) and (b₂) taken from the cross section, (c₁) and (c₂) taken from the surface. (TA: Tensile axis, IPF: Inverse pole figure, KAM: Kernel average misorientation).

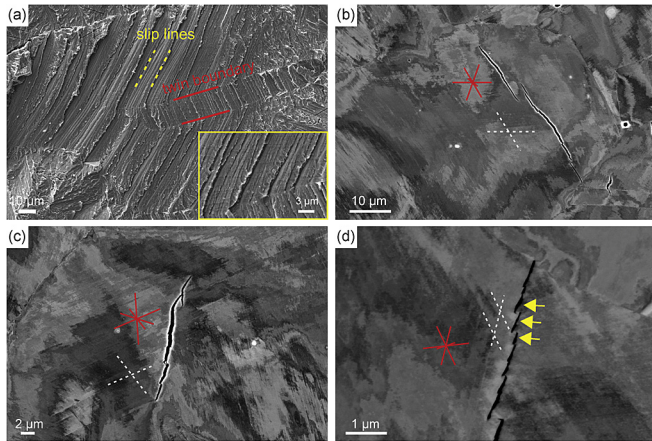


Fig. 8. Hydrogen-induced cracking in the as WQ sample: (a) fracture surface, (b)–(d) ECC images showing transgranular cracks (images taken from the surface). Dashed white lines indicate the observed slip lines, and red lines indicate the {111} plane traces obtained from EBSD measurements. (For interpretation of the references to colour in this figure legend, the reader is referred to the web version of this article.)

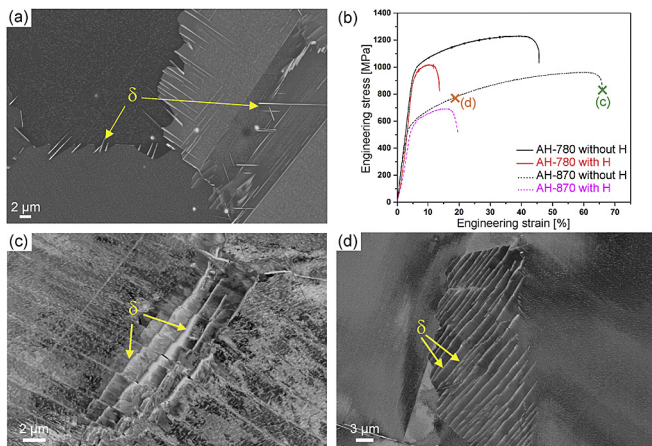


Fig. 9. AH-870 (aged at 870 °C) (a) BSE image of the undeformed sample. (b) Engineering stress-strain curves, with and without H-charging, in comparison with AH-780 (age-hardened at 780 °C). Deformation microstructures without H-charging: (c) fractured sample, (d) deformed till 17% strain (images taken from the surface).

Observations on the fracture surfaces of the hydrogen charged samples indicated an increase in the fraction of transgranular failure (Fig. 10a). Postmortem microstructural observations on the samples that had failed in the presence of hydrogen showed cracks that also propagated along the δ -phase inside the grains (intragranular δ -phase). Fig. 10b and c shows a crack following the intragranular δ . It is clearly observed that the precipitation-free zones are extended along the δ phase into the grain interior. High strain localization was observed in the precipitation-free zones around δ -precipitates (Fig. 10c).

4. Discussion

4.1. Deformation mode without the presence of hydrogen

A planar mode of plastic deformation was observed in both, age-hardened (AH-780) and as water quenched (as WQ) states. Planar arrangements of dislocations were clearly visible in the ECC images of the deformed as WQ state (Fig. 7d). Since alloy 718 is a medium stacking fault energy (SFE) Ni-based superalloy

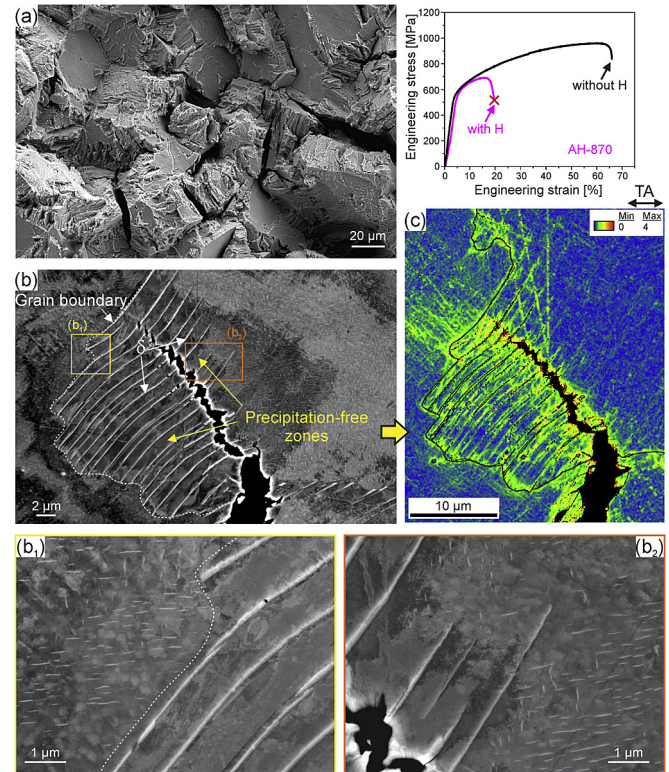


Fig. 10. Hydrogen-assisted fracture in AH-870: (a) Fracture surface, (b) ECC image of a crack propagated along intragranular δ , and (c) the corresponding KAM map (step size: 100 nm). The black lines indicate the high angle GBs. (b_1) and (b_2) magnified regions marked in (b). The images and the EBSD scan are taken from the surface. (TA: Tensile axis, KAM: Kernel average misorientation).

(SFE = 50–75 mJ m⁻²), it promotes a trend for developing planar deformation substructures. Unalloyed Ni has a high SFE (120–130 mJ m⁻²) and thus develops a dislocation cell structure during deformation [14]. The substantially lower SFE in alloy 718 relative to that of pure Ni (due to high alloying additions), thus might promote planar dislocation patterning features. More importantly shearing of ordered precipitates in the age-hardened state and short range clustering in the as WQ state are suggested to be the main causes for planar deformation in these materials [14–16].

As mentioned above the underlying deformation mechanisms of structural alloys strongly influence their HE susceptibility. Alloys deforming predominantly by planar slip are equipped with a larger intrinsic propensity for localized deformation. It has been shown that these alloys are more susceptible to hydrogen damaging effects compared to materials which deform with more homogeneous slip modes [10,11]. In the light of these earlier observations we hence suggest that the current alloy with its different microstructure features promoting planar slip (SFE, shearable precipitates, ordered clusters) creates higher local stresses at the localization zones, rendering the alloy more susceptible to HE.

4.2. Hydrogen uptake during slow strain rate tensile testing under in situ H-charging

It has been shown that the HE susceptibility of alloy 718 is strain rate sensitive and is more pronounced at very slow strain rates (5×10^{-7} s⁻¹) and almost disappears at a more modest strain rate of 5×10^{-3} s⁻¹ [2]. Hence it has been suggested that HE is associated with hydrogen segregation to mobile dislocations, which

occurs more readily at low deformation rates and the associated low dislocation velocities [2]. In our approach tensile testing under hydrogen charging at a strain rate of 10^{-4} s^{-1} led to a distinct reduction in ductility and revealed severe HE in alloy 718. In this way, hydrogen-decorated dislocations assisted the hydrogen transport within the samples in addition to the diffusion process [35,36].

The hydrogen diffusion depth can be estimated roughly by \sqrt{Dt} , where D is the diffusion coefficient and t is the hydrogen charging time. The diffusion coefficient of hydrogen in alloy 718 in the age-hardened state was reported to be $1.4 \times 10^{-15} \text{ m}^2 \text{ s}^{-1}$ at room temperature [37]. Hence, a considerable time is required to achieve a fully hydrogen-saturated sample with 1 mm thickness via diffusion at room temperature. Considering hydrogen transport solely by lattice diffusion, the hydrogen-diffusion depth after 4 h pre-charging plus additional 20 min of tensile test duration is estimated as $\sim 4.7 \text{ }\mu\text{m}$ in AH-780 sample. The measured hydrogen-affected zone obtained from analyzing the fracture surfaces (depth of the embrittled area) in AH-780 was $\sim 200 \text{ }\mu\text{m}$ (Fig. 4a). Also, comparison of the TD curves of the pre-charged sample and the sample deformed in situ during ongoing hydrogen charging showed a significant increase in the hydrogen content (13 wt. ppm and 40 wt. ppm, respectively). It should be also considered that surface cracks forming during the deformation further enhance the hydrogen uptake by increasing the available free surface area.

The depth of the hydrogen-affected zone was much higher in the as WQ case ($\sim 400 \text{ }\mu\text{m}$). Although the diffusion coefficient in the solution annealed state was reported to be slightly higher ($1.9 \times 10^{-15} \text{ m}^2 \text{ s}^{-1}$, at room temperature) [37], the hydrogen-diffusion depth by pure lattice diffusion is estimated to be $5.8 \text{ }\mu\text{m}$ (considering 4 h pre-charging and tensile test duration of 1 h). Obviously, higher ductility and hence longer tensile test duration ($\sim 1 \text{ h}$) led to further hydrogen transport via dislocations and consequently deeper embrittled area. The contribution of both, the hydrogen transport by dislocations and the occurrence of surface cracks during deformation led to hydrogen distributions that most likely extended farther into the specimen than expected by classical bulk diffusion [36]. This phenomenon was indeed revealed by the increase in the hydrogen concentration and the extent of the observed embrittled zone.

4.3. Hydrogen-assisted cracking mechanisms

Analysis of AH-780 sample showed $\sim 45\%$ tensile elongation and ductile fracture behavior when not charged by hydrogen. The elongation to fracture was drastically reduced by hydrogen uptake to $\sim 12\%$. The associated fracture surfaces showed characteristics of intergranular and transgranular modes of failure. The as WQ material also showed susceptibility to HE. Although the elongation to fracture in the presence of hydrogen was still considerable ($\sim 30\%$), the value was reduced by $\sim 70\%$ relative to the non hydrogen charged sample. In this case HE occurred already at a surprisingly low strength level (400 MPa yield strength) and without the presence of intermetallic precipitates (γ'/γ'' and δ). Changes in heat treatments affected the precipitation conditions and consequently the material's strength and ductility. Also differences in test conditions such as hydrogen charging time occurred due to different test durations. These factors influenced the hydrogen transport and uptake. Hence, the values of the reduction in ductility are not directly quantitatively comparable among samples subjected to different heat treatments. The observed cracking mechanisms are compared and discussed in the following.

4.3.1. Hydrogen-assisted transgranular cracking

Hydrogen-induced transgranular cracking was observed in

both, the age-hardened AH-780 (Fig. 6) and as WQ (Fig. 8) states. Additionally, fracture surfaces showed characteristics of quasi-cleavage failure with striations, composed of ridges, running approximately parallel to the crack propagation direction (Fig. 8a). Quasi-cleavage is a common observed feature in hydrogen-induced fracture surfaces and is generally defined as a cleavage-like fracture but not along a known cleavage plane [38]. Appearance of quasi-cleavage fracture along dislocation slip lines has been explained based on enhanced plasticity in the presence of hydrogen (HELP mechanism) resulting in shear localization zones along slip planes [38,39]. Post mortem microstructural observations showed cracks along slip bands (Figs. 6a and 8b), in the form of 'zig-zag' shaped cracks running along alternating $\{111\}$ slip planes (Fig. 6b₁,b₂ and Fig. 8c and d), and as cracks with growth directions on $\{100\}$ planes near $\langle 110 \rangle$ crystallographic directions (Fig. 6c₁,c₂). The enhanced localized deformation by hydrogen is due to the fact that hydrogen stabilizes the edge component of mixed dislocations [40], promoting planar slip at the expense of cross slip. Also reduction of stacking fault energy by hydrogen increases the separation of partials leading to inhibited cross slip and thus hydrogen-induced slip planarity [41–43]. Cross slip suppression and enhanced slip planarity due to hydrogen, result in strain concentration within the deformation bands [24]. Hydrogen-induced cracking along slip bands has been frequently observed in materials with an inherent tendency for planar slip, e.g., in stainless steels, Fe-Mn-C based steels, and Ni-based superalloys [10,11,30,44,45].

Deviations from specific crack paths along low-index crystallographic planes and directions will arise, if unequal amounts of dislocation slip occur on each crack side due to corresponding differences in the shear stresses on the different competing slip planes [44]. When the crack-tip resolved shear stress intensity factor (K_{RSS}) pertaining to one active slip system is much higher than that of all other slip systems, crack propagates on a single $\{111\}$ slip plane. When the K_{RSS} values of two intersecting conjugate $\{111\}$ slip systems are comparable, crack growth alternates between the two active slip planes, resulting in a non-slip-plane $\{100\}$ crack surface bisecting the two active slip planes. While the microscopic cracking plane always follows the $\{111\}$ planes, the resultant macroscopic crack plane remains on the $\{100\}$ plane (Fig. 6c₁,c₂) [46].

4.3.2. Damage by void formation and coalescence

Observation of saw-teeth shaped features along the tear ridges on the fracture surface (Fig. 8a) indicates the occurrence of fracture by accelerated and localized plastic slip processes rather than by conventional cleavage [38]. Also, Fig. 8d is an indication of void widening and growth along intersecting slip lines as the crack initiation.

Shear localization due to the presence of hydrogen is associated with localized ductile fracture [21,23]. Ductile fracture assumes initiation, growth, and coalescence of voids, and ductile crack growth resistance is determined by the distribution of nucleating voids and the stress state in the crack front [47]. Increased strain levels within slip bands lead to void initiation at lower global strains [44]. Voids or microcracks initiate at slip band intersections due to associated inhomogeneous strain distribution, dislocation reactions, local stress peaks, and the resulting local hydrogen concentration at such spots [38,39]. Voids will grow both, by a diffusive process and by conventional plasticity (dislocation processes), if the local stresses are high enough [19,39,44]. Once the number or the size of the voids reach a critical level, the shear localization becomes autocatalytic, resulting in fracture along the deformation substructure features [19,38,39,44]. Results of Zhang et al. [6] reported for alloy 718, also showed nano-voids coalescence as the prevalent mechanism leading to crack propagation along slip

lines.

It is well known that hydrogen reduces the vacancy formation energy [44,48,49]. Also, there is a substantial increase in the vacancy concentration due to plastic deformation, which is also enhanced in the presence of hydrogen [49]. Based on the extensive discussion on the vacancy-driven mechanism for void nucleation that exists in the literature [39,50–52], it is reasonable to expect in the current case, that nano-voids can nucleate and grow in the presence of hydrogen-stabilized excess vacancies. When they collapse into small clusters they form embryos of nano-voids. These nano-voids develop further into regular voids via ongoing vacancy condensation and dislocation slip in the stress concentration regions around them. Deformation driven void coalescence, enhanced local plastic slip in the stress concentration zones between the voids, and decrease in the ductile crack growth resistance then follow. This can be regarded as a kind of “internal necking” and leads to enhanced shear localization and premature failure.

Since the formation of strain-induced vacancies results from interactions between dislocations, HE should be sensitive to local situations with high dislocation densities such as within slip bands or in pile-up regions close to GBs [48], making these sites as favorable damage initiation sites.

4.3.3. Hydrogen-assisted intergranular cracking

Hydrogen-induced intergranular cracking was observed in the age-hardened material (AH-780) at γ/γ GBs, GB triple junctions, and at δ -decorated GBs (Fig. 5). The yield strength, GB segregation, and hydrogen fugacity are important factors in controlling intergranular cracking [29]. High strain localization occurred at the GBs of the deformed samples, especially at the points of intersection with the slip bands (Figs. 3b, 3d₂, 5a₂, b₂). Plasticity plays an important role in hydrogen-induced intergranular failure. Deformation processes lead to stress localization through work hardening and also establish high hydrogen concentrations at GBs, thereby facilitating decohesion and crack nucleation [53]. Additionally large elastic misfit at GB triple junctions assists cracking at an early stage of deformation [30]. Intergranular fracture due to strain localization and concurrent void formation was also observed in case of a precipitation hardened- and a metastable austenitic steel [30] [54].

Observations on two aging states of alloy 718 (AH-780 and AH-870) with different precipitation conditions of the δ -phase showed that δ promotes HE by initializing micro-cracks. Additionally, local softening in the precipitation-free zones around δ enhanced strain localization (Fig. 10c). In a previous study [55] we performed multiscale and spatially resolved hydrogen mapping on an electrochemically hydrogen charged binary Ni-Nb model alloy. By correlating the results with mechanical testing, we showed that hydrogen-enhanced decohesion (HEDE) occurring at γ/δ interfaces was the embrittlement mechanism in the hydrogen charged samples. Hydrogen accumulation at γ/δ interfaces under applied loads led to reduction in the bonding strength and concurrent decohesion during straining [55]. Based on the current results and the previous study, it is concluded that GBs decorated with δ -phase are more prone to crack initiation and propagation in the presence of hydrogen, i.e. GB δ -phase promotes/assists hydrogen-induced intergranular cracking.

Contrary to the present results, showing the occurrence of hydrogen-induced intergranular cracking in AH-780, Zhang et al. [6] reported no incident of intergranular cracking in electrochemically hydrogen pre-charged and tensile tested alloy 718. This discrepancy among the two sets of observations could be due to different factors such as differences in bulk chemical compositions, hydrogen chemical potential, heat treatments, and test conditions.

The yield strengths of the investigated alloys in both studies are comparable (~ 1000 MPa). Also, the much lower strain rate imposed in their case (100 times lower than in our present study) is expected to enhance the hydrogen effects. However, the most important difference between the two studies lies in the choice of the respective hydrogen charging modes. The hydrogen content was not reported in the former study, but we showed that the here used in situ tensile testing under hydrogen charging leads to much higher hydrogen uptake by the material compared to conventional pre-charging. As mentioned above a critical hydrogen concentration has to be reached at the GB, causing intergranular fracture. GB diffusion of hydrogen controls the kinetics of intergranular embrittlement. With permanent hydrogen supply at an external surface, the kinetics of intergranular embrittlement is faster than can be accounted for by lattice diffusion of hydrogen [56]. It is believed that by in situ tensile testing under constant hydrogen charging the critical hydrogen concentration was attained at GBs, leading to accelerated decohesion and crack propagation.

The as WQ material with 400 MPa yield strength showed no intergranular cracking after fracture in the presence of hydrogen. Since the equilibrium hydrogen concentration at the region of maximum stress varies exponentially with the yield stress [29], this low strength level did not result in high stress concentration and hydrogen accumulation at GBs, favoring crack propagation. Another important factor in controlling intergranular fracture is GB segregation [29,57]. For example sulfur segregation at GBs was shown to enhance intergranular HE in case of pure Ni [58]. GB segregation was not investigated in this study, but previous investigations have reported segregation of elements such as S, P, B, C, Mo, and Nb at GBs in alloy 718, with the segregation being more pronounced upon slow cooling [59–61]. Although not a focus of the present study, it should be considered that each segregated impurity element has an embrittling potency and specific influence on GB diffusivity. For example in Ni and Ni-alloys, B and C increase GB cohesion, while S segregation has a negative effect and increases the amount of embrittlement [56,62]. These parameters together with the nature of the GB and stress conditions, affect the critical concentration of segregating elements plus hydrogen, required for embrittlement [63]. It is believed that segregation was inhibited in the as WQ state, due to insufficient time for diffusion of vacancy-solute complexes in an austenitic structure with slow diffusion rate [64]. It is concluded that due to the combined effects of limited GB segregation, absence of GB δ -phase, and low flow stress, the cohesive strength of the GB was not reached at the as WQ condition.

4.4. Summary of hydrogen-assisted cracking mechanisms

Fig. 11 summarizes schematically the different types of observed cracking mechanisms in alloy 718. The impingement of {111} slip bands at an obstacle, such as an intersecting slip band (Fig. 11a–c) or a GB (Fig. 11d) causes local stress concentrations and strain discontinuities at the intersection points. Hydrogen is attracted more to the regions with higher local stress (correspondingly higher dislocation density). Hence, plastic instabilities arise in regions of localized/heterogeneous deformation with non-uniform hydrogen concentrations, leading to void initiation as primary damage sites. Voids growth and coalescence through dislocation processes lead to final failure [8,44].

Comparison between hydrogen-related failure of the two states before and after age-hardening (as WQ and AH-780, respectively) with different strength levels clearly showed the change of the acting fracture modes due to the occurrence of different strain- and/or stress-controlled cracking mechanisms. Although not the focus of the current study; it is important to consider that by

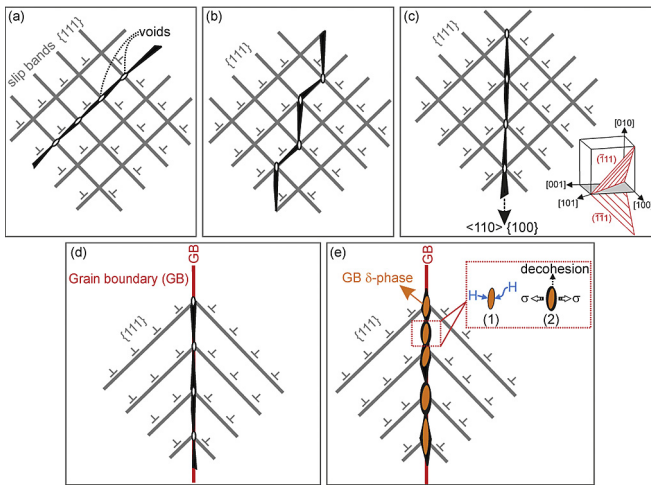


Fig. 11. Schematics showing localized deformation leading to cracks: (a) along slip band, (b) along alternating slip bands, (c) on {100} plane following $\langle 110 \rangle$ direction at intersection of slip bands. (d) stress-assisted grain boundary cracking, (e) δ -decohesion-assisted cracking of δ -decorated grain boundary.

changing the precipitation conditions, the precipitate volume fractions, size, and coherency are affected, which further influence hydrogen diffusivity, uptake, and trapping behavior. According to the present results and since the HE occurred even in the precipitation-free condition (as WQ, without γ'/γ'' and δ), it seems that the deformation modes affecting the stress and/or strain localization have a more pronounced effect.

5. Conclusions

Hydrogen effects on the tensile ductility of alloy 718 were investigated in the solution annealed and age-hardened states by tensile testing under in situ hydrogen charging:

1. Embrittlement occurred by strong hydrogen-deformation interactions. Fracture in hydrogen charged samples was dominated by localized deformation. Stress concentrations and/or strain discontinuities at the impingement of slip bands at grain boundaries and/or at intersecting slip bands led to crack formation.
2. Strain-controlled transgranular cracking leading to quasi-cleavage fracture was observed in both, solution annealed and age-hardened materials when hydrogen was present during deformation. Transgranular cracking was caused by HELP-assisted shear localization and void nucleation and coalescence along $\{111\}$ slip planes.
3. Intergranular cracking was observed in the age-hardened material (1000 MPa yield strength) due to grain boundary triple junction cracking, slip-localization along γ/γ' grain boundaries, and δ/γ -matrix interface cracking.
4. The absence of intergranular cracking in the solution annealed state was attributed to the low yield strength (400 MPa), limited segregation, and absence of δ -phase at grain boundaries.

Acknowledgments

ZT gratefully acknowledges the support of VDM Metals GmbH, Germany. M. Koyama is gratefully acknowledged for helpful discussions.

References

- [1] J.J. Debarbadillo, S.K. Mannan, Alloy 718 for oilfield applications, *J. Met.* 64 (2012) 265–270, <http://dx.doi.org/10.1007/s11837-012-0238-z>.
- [2] L. Fournier, D. Delafosse, T. Magnin, Cathodic hydrogen embrittlement in alloy 718, *Mater. Sci. Eng. A* 269 (1999) 111–119, [http://dx.doi.org/10.1016/S0921-5093\(99\)00167-7](http://dx.doi.org/10.1016/S0921-5093(99)00167-7).
- [3] L. Liu, K. Tanaka, A. Hirose, K.F. Kobayashi, Effects of precipitation phases on the hydrogen embrittlement sensitivity of Inconel 718, *Sci. Technol. Adv. Mater.* 3 (2002) 335–344, [http://dx.doi.org/10.1016/S1468-6996\(02\)00039-6](http://dx.doi.org/10.1016/S1468-6996(02)00039-6).
- [4] F. Galliano, E. Andrieu, C. Blanc, J.M. Cloue, D. Connetable, G. Odemer, Effect of trapping and temperature on the hydrogen embrittlement susceptibility of alloy 718, *Mater. Sci. Eng. A* 611 (2014) 370–382, <http://dx.doi.org/10.1016/j.msea.2014.06.015>.
- [5] M.C. Rezende, L.S. Araujo, S.B. Gabriel, D.S. dos Santos, L.H. de Almeida, Hydrogen embrittlement in nickel-based superalloy 718: relationship between $\gamma' + \gamma''$ precipitation and the fracture mode, *Int. J. Hydrogen Energy* 40 (2015) 17075–17083, <http://dx.doi.org/10.1016/j.ijhydene.2015.07.053>.
- [6] Z. Zhang, G. Obasi, R. Morana, M. Preuss, Hydrogen assisted crack initiation and propagation in a nickel-based superalloy, *Acta Mater.* 113 (2016) 272–283, <http://dx.doi.org/10.1016/j.actamat.2016.05.003>.
- [7] R.C. Reed, *The superalloys: Fundamentals and Applications*, Cambridge University Press, 2006.
- [8] K.A. Nibur, B.P. Somerday, D.K. Balch, C. San Marchi, The role of localized deformation in hydrogen-assisted crack propagation in 21Cr-6Ni-9Mn stainless steel, *Acta Mater.* 57 (2009) 3795–3809, <http://dx.doi.org/10.1016/j.actamat.2009.04.027>.
- [9] M. Koyama, E. Akiyama, K. Tsuzaki, D. Raabe, Hydrogen-assisted failure in a twinning-induced plasticity steel studied under in situ hydrogen charging by electron channeling contrast imaging, *Acta Mater.* 61 (2013) 4607–4618, <http://dx.doi.org/10.1016/j.actamat.2013.04.030>.
- [10] Z. Guo, M. Zhao, C. Li, S. Chen, L. Rong, Mechanism of hydrogen embrittlement in a gamma-prime phase strengthened Fe-Ni based austenitic alloy, *Mater. Sci. Eng. A* 555 (2012) 77–84, <http://dx.doi.org/10.1016/j.msea.2012.06.036>.
- [11] T. Michler, J. Naumann, M.P. Balogh, Hydrogen environment embrittlement of solution treated Fe-Cr-Ni super alloys, *Mater. Sci. Eng. A* 607 (2014) 71–80, <http://dx.doi.org/10.1016/j.msea.2014.03.134>.
- [12] M. Koyama, E. Akiyama, T. Sawaguchi, D. Raabe, K. Tsuzaki, Hydrogen-induced cracking at grain and twin boundaries in an Fe-Mn-C austenitic steel, *Scr. Mater.* 66 (2012) 459–462, <http://dx.doi.org/10.1016/j.scriptamat.2011.12.015>.
- [13] D.W. Worthem, I.M. Robertson, F.A. Leckie, D.F. Socie, C.J. Altstetter, Inhomogeneous deformation in INCONEL 718 during monotonic and cyclic loadings, *Metall. Trans. A* 21 (1990) 3215–3220, <http://dx.doi.org/10.1007/BF02647316>.
- [14] M. Sundararaman, P. Mukhopadhyay, S. Banerjee, Deformation behaviour of γ'' strengthened Inconel 718, *Acta Metall.* 36 (1988) 847–864, [http://dx.doi.org/10.1016/0001-6160\(88\)90139-3](http://dx.doi.org/10.1016/0001-6160(88)90139-3).
- [15] L. Xiao, D.L. Chen, M.C. Chaturvedi, Shearing of gamma double prime precipitates and formation of planar slip bands in Inconel 718 during cyclic deformation, *Scr. Mater.* 52 (2005) 603–607, <http://dx.doi.org/10.1016/j.scriptamat.2004.11.023>.
- [16] V. Gerold, H.P. Karnthaler, On the origin of planar slip in f.c.c. alloys, *Acta Metall.* 37 (1989) 2177–2183, [http://dx.doi.org/10.1016/0001-6160\(89\)90143-0](http://dx.doi.org/10.1016/0001-6160(89)90143-0).
- [17] R. Kirchheim, Reducing grain boundary, dislocation line and vacancy formation energies by solute segregation. I. Theoretical background, *Acta Mater.* 55 (2007) 5129–5138, <http://dx.doi.org/10.1016/j.actamat.2007.05.047>.
- [18] R. Kirchheim, Reducing grain boundary, dislocation line and vacancy formation energies by solute segregation II. Experimental evidence and consequences, *Acta Mater.* 55 (2007) 5139–5148, <http://dx.doi.org/10.1016/j.actamat.2007.05.033>.
- [19] R. Kirchheim, B. Somerday, P. Sofronis, Chemomechanical effects on the separation of interfaces occurring during fracture with emphasis on the hydrogen-iron and hydrogen-nickel system, *Acta Mater.* 99 (2015) 87–98, <http://dx.doi.org/10.1016/j.actamat.2015.07.057>.
- [20] P. Rozenak, I.M. Robertson, H.K. Birnbaum, HVEM studies of the effects of hydrogen on the deformation and fracture of AISI type 316 austenitic stainless steel, *Acta Metall. Mater.* 38 (1990) 2031–2040, [http://dx.doi.org/10.1016/0956-7151\(90\)90070-W](http://dx.doi.org/10.1016/0956-7151(90)90070-W).
- [21] H.K. Birnbaum, P. Sofronis, Hydrogen-enhanced localized plasticity—a mechanism for hydrogen-related fracture, *Mater. Sci. Eng. A* 176 (1994) 191–202, [http://dx.doi.org/10.1016/0921-5093\(94\)90975-X](http://dx.doi.org/10.1016/0921-5093(94)90975-X).
- [22] P.J. Ferreira, I.M. Robertson, H.K. Birnbaum, Hydrogen effects on the interaction between dislocations, *Acta Mater.* 46 (1998) 1749–1757, [http://dx.doi.org/10.1016/S1359-6454\(97\)00349-2](http://dx.doi.org/10.1016/S1359-6454(97)00349-2).
- [23] P. Sofronis, Y. Liang, N. Aravas, Hydrogen induced shear localization of the plastic flow in metals and alloys, *Eur. J. Mech. - A/Solids* 20 (2001) 857–872, [http://dx.doi.org/10.1016/S0997-7538\(01\)00179-2](http://dx.doi.org/10.1016/S0997-7538(01)00179-2).
- [24] I.M. Robertson, The effect of hydrogen on dislocation dynamics, *Eng. Fract. Mech.* 68 (2001) 671–692, [http://dx.doi.org/10.1016/S0013-7944\(01\)00011-X](http://dx.doi.org/10.1016/S0013-7944(01)00011-X).
- [25] P. Sofronis, H.K. Birnbaum, Mechanics of the hydrogen-dislocation-impurity interactions—I. Increasing shear modulus, *J. Mech. Phys. Solids* 43 (1995)

- 49–90, [http://dx.doi.org/10.1016/0022-5096\(94\)00056-B](http://dx.doi.org/10.1016/0022-5096(94)00056-B).
- [26] J.P. Chateau, D. Delafosse, T. Magnin, Numerical simulations of hydrogen–dislocation interactions in fcc stainless steels. Part I: hydrogen–dislocation interactions in bulk crystals, *Acta Mater* 50 (2002) 1507–1522, [http://dx.doi.org/10.1016/S1359-6454\(02\)00008-3](http://dx.doi.org/10.1016/S1359-6454(02)00008-3).
- [27] D.C. Ahn, P. Sofronis, R. Dodds, Modeling of hydrogen-assisted ductile crack propagation in metals and alloys, *Int. J. Fract.* 145 (2007) 135–157, <http://dx.doi.org/10.1007/s10704-007-9112-3>.
- [28] I.M. Robertson, H.K. Birnbaum, P. Sofronis, Hydrogen Effects on Plasticity, *Dislocations in Solids*, 15, 2009, pp. 249–293.
- [29] C.J. McMahon, Hydrogen-induced intergranular fracture of steels, *Eng. Fract. Mech.* 68 (2001) 773–788, [http://dx.doi.org/10.1016/S0013-7944\(00\)00124-7](http://dx.doi.org/10.1016/S0013-7944(00)00124-7).
- [30] M. Koyama, H. Springer, S.V. Merzlikin, K. Tsuzaki, E. Akiyama, D. Raabe, Hydrogen embrittlement associated with strain localization in a precipitation-hardened Fe–Mn–Al–C light weight austenitic steel, *Int. J. Hydrogen Energy* 39 (2014) 4634–4646, <http://dx.doi.org/10.1016/j.ijhydene.2013.12.171>.
- [31] L.N. Brewer, D.P. Field, C.C. Merriman, Mapping and assessing plastic deformation using EBSD, in: *Electron Backscatter Diffraction*, Mater. Sci., Springer, 2009, pp. 251–262.
- [32] I. Gutierrez-Urrutia, S. Zaefferer, D. Raabe, Coupling of electron channeling with EBSD: toward the quantitative characterization of deformation structures in the sem, *Jom* 65 (2013) 1229–1236, <http://dx.doi.org/10.1007/s11837-013-0678-0>.
- [33] I. Gutierrez-Urrutia, S. Zaefferer, D. Raabe, Electron channeling contrast imaging of twins and dislocations in twinning-induced plasticity steels under controlled diffraction conditions in a scanning electron microscope, *Scr. Mater* 61 (2009) 737–740, <http://dx.doi.org/10.1016/j.scriptamat.2009.06.018>.
- [34] S. Zaefferer, N. Elhami, Theory and application of electron channelling contrast imaging under controlled diffraction conditions, *Acta Mater* 75 (2014) 20–50, <http://dx.doi.org/10.1016/j.actamat.2014.04.018>.
- [35] J. Tien, A.W. Thompson, I.M. Bernstein, R.J. Richards, Hydrogen transport by dislocations, *Metall. Trans. A* 7 (1976) 821–829, <http://dx.doi.org/10.1007/BF02644079>.
- [36] M. Dadfarina, M.L. Martin, A. Nagao, P. Sofronis, I.M. Robertson, Modeling hydrogen transport by dislocations, *J. Mech. Phys. Solids* 78 (2015) 511–525, <http://dx.doi.org/10.1016/j.jmps.2015.03.002>.
- [37] W.M. Robertson, Hydrogen permeation and diffusion in inconel 718 and incoloy 903, *Metall. Trans. A* 8 (1977) 1709–1712, <http://dx.doi.org/10.1007/BF02646873>.
- [38] M.L. Martin, J.A. Fenske, G.S. Liu, P. Sofronis, I.M. Robertson, On the formation and nature of quasi-cleavage fracture surfaces in hydrogen embrittled steels, *Acta Mater* 59 (2011) 1601–1606, <http://dx.doi.org/10.1016/j.actamat.2010.11.024>.
- [39] T. Neeraj, R. Srinivasan, J. Li, Hydrogen embrittlement of ferritic steels: observations on deformation microstructure, nanoscale dimples and failure by nanovoiding, *Acta Mater* 60 (2012) 5160–5171, <http://dx.doi.org/10.1016/j.actamat.2012.06.014>.
- [40] P.J. Ferreira, I.M. Robertson, H.K. Birnbaum, Hydrogen effects on the character of dislocations in high-purity aluminum, *Acta Mater* 47 (1999) 2991–2998, [http://dx.doi.org/10.1016/S1359-6454\(99\)00156-1](http://dx.doi.org/10.1016/S1359-6454(99)00156-1).
- [41] M. Wen, S. Fukuyama, K. Yokogawa, Cross-slip process in fcc nickel with hydrogen in a stacking fault: an atomistic study using the embedded-atom method, *Phys. Rev. B - Condens. Matter Mater. Phys.* 75 (2007) 24–28, <http://dx.doi.org/10.1103/PhysRevB.75.144110>.
- [42] M. Wen, S. Fukuyama, K. Yokogawa, Atomistic simulations of hydrogen effect on dissociation of screw dislocations in nickel, *Scr. Mater* 52 (2005) 959–962, <http://dx.doi.org/10.1016/j.scriptamat.2005.01.044>.
- [43] A. Barnoush, H. Vehoff, In situ electrochemical nanoindentation: a technique for local examination of hydrogen embrittlement, *Corros. Sci.* 50 (2008) 259–267, <http://dx.doi.org/10.1016/j.corsci.2007.05.026>.
- [44] S. Lynch, Hydrogen embrittlement phenomena and mechanisms, *Corros. Rev.* 30 (2012) 105–123, <http://dx.doi.org/10.1515/corrrev-2012-0502>.
- [45] C. Borchers, T. Michler, A. Pundt, Effect of hydrogen on the mechanical properties of stainless steels, *Adv. Eng. Mater* 10 (2008) 11–23, <http://dx.doi.org/10.1002/adem.200700252>.
- [46] Q. Chen, W. Liu, Shear Fatigue Crack Growth in Large Grain Polycrystals, in: F. Erdogan (Ed.), *Fract. Mech.* 25th Vol. ASTM STP 1220, American Society for Testing and Materials, 1995.
- [47] M. Nagumo, Function of hydrogen in embrittlement of high-strength steels, *ISIJ Int.* 41 (2001) 590–598, <http://dx.doi.org/10.2355/isijinternational.41.590>.
- [48] M. Nagumo, Hydrogen related failure of steels – a new aspect, *Mater. Sci. Technol.* 20 (2004) 940–950, <http://dx.doi.org/10.1179/026708304225019687>.
- [49] M. Nagumo, K. Takai, N. Okuda, Nature of hydrogen trapping sites in steels induced by plastic deformation, *J. Alloys Compd.* 293 (1999) 310–316, [http://dx.doi.org/10.1016/S0925-8388\(99\)00322-9](http://dx.doi.org/10.1016/S0925-8388(99)00322-9).
- [50] Q.-Z. Chen, W.-Y. Chu, Y.-B. Wang, C.-M. Hsiao, In situ TEM observations of nucleation and bluntness of nanocracks in thin crystals of 310 stainless steel, *Acta Metall. Mater* 43 (1995) 4371–4376, [http://dx.doi.org/10.1016/0956-7151\(95\)00122-C](http://dx.doi.org/10.1016/0956-7151(95)00122-C).
- [51] A.M. Cuitiño, M. Ortiz, Ductile fracture by vacancy condensation in F.C.C. single crystals, *Acta Mater* 44 (1996) 427–436, [http://dx.doi.org/10.1016/1359-6454\(95\)00220-0](http://dx.doi.org/10.1016/1359-6454(95)00220-0).
- [52] E.M. Bringa, S. Traiviratana, M.A. Meyers, Void initiation in fcc metals: effect of loading orientation and nanocrystalline effects, *Acta Mater* 58 (2010) 4458–4477.
- [53] M.L. Martin, B.P. Somerday, R.O. Ritchie, P. Sofronis, I.M. Robertson, Hydrogen-induced intergranular failure in nickel revisited, *Acta Mater* 60 (2012) 2739–2745, <http://dx.doi.org/10.1016/j.actamat.2012.01.040>.
- [54] A. Macadre, N. Nakada, T. Tsuchiyama, S. Takaki, Critical grain size to limit the hydrogen-induced ductility drop in a metastable austenitic steel, *Int. J. Hydrogen Energy* 40 (2015) 10697–10703, <http://dx.doi.org/10.1016/j.ijhydene.2015.06.111>.
- [55] Z. Tarzimaghadam, M. Rohwerder, S.V. Merzlikin, A. Bashir, L. Yedra, S. Eswara, et al., Multi-scale and spatially resolved hydrogen mapping in a Ni–Nb model alloy reveals the role of the δ phase in hydrogen embrittlement of alloy 718, *Acta Mater* 109 (2016) 69–81, <http://dx.doi.org/10.1016/j.actamat.2016.02.053>.
- [56] A. Kimura, H.K. Birnbaum, Hydrogen induced grain boundary fracture in high purity nickel and its alloys-Enhanced hydrogen diffusion along grain boundaries, *Acta Metall.* 36 (1988) 757–766, [http://dx.doi.org/10.1016/0001-6160\(88\)90109-5](http://dx.doi.org/10.1016/0001-6160(88)90109-5).
- [57] D. Raabe, M. Herbig, S. Sandlöbes, Y. Li, D. Tytko, M. Kuzmina, et al., Grain boundary segregation engineering in metallic alloys: A pathway to the design of interfaces 18 (2014) 253–261, <http://dx.doi.org/10.1016/j.cossms.2014.06.002>.
- [58] D.H. Lassila, H.K. Birnbaum, Intergranular fracture of nickel: the effect of hydrogen-sulfur co-segregation, *Acta Met.* 35 (1987) 1815–1822.
- [59] J. Dong, M. Zhang, X. Xie, R.G. Thompson, Interfacial segregation and cosegregation behaviour in a nickel-base alloy 718 (328) (2002) 8–13.
- [60] D.H. Ping, Y.F. Gu, C.Y. Cui, H. Harada, Grain boundary segregation in a Ni – Fe-based (Alloy 718) superalloy 456 (2007) 99–102, <http://dx.doi.org/10.1016/j.jmse.2007.01.090>.
- [61] W. Chen, M.C. Chaturvedi, N.L. Richards, G. McMahon, Grain boundary segregation of boron in INCONEL 718, *Metall. Mater. Trans. A* 29 (1998) 1947–1954.
- [62] V.I. Razumovskiy, A.Y. Lozovoi, I.M. Razumovskii, First-principles-aided design of a new Ni-base superalloy: influence of transition metal alloying elements on grain boundary and bulk cohesion, *Acta Mater* 82 (2015) 369–377, <http://dx.doi.org/10.1016/j.actamat.2014.08.047>.
- [63] S.M. Brummer, R.H. Jones, M.T. Thomas, D.R. Baer, Influence of sulfur, phosphorus, and antimony segregation on the intergranular hydrogen embrittlement of nickel, *Metall. Trans. A* 14A (1983) 223–232.
- [64] X. Huang, M.C. Chaturvedi, N.L. Richards, J. Jackman, The effect of grain boundary segregation of boron in cast alloy 718 on HAZ microfissuring-A SIMS analysis, *Acta Mater* 45 (1997) 3095–3107.